

## New Efficient Sparse Space–Time Algorithms for Superparameterization on Mesoscales

YULONG XING AND ANDREW J. MAJDA

*Department of Mathematics and Climate, Atmosphere and Ocean Science, Courant Institute of Mathematical Sciences, New York University, New York, New York*

WOJCIECH W. GRABOWSKI

*National Center for Atmospheric Research,\* Boulder, Colorado*

(Manuscript received 13 November 2008, in final form 26 May 2009)

### ABSTRACT

Superparameterization (SP) is a large-scale modeling system with explicit representation of small-scale and mesoscale processes provided by a cloud-resolving model (CRM) embedded in each column of a large-scale model. New efficient sparse space–time algorithms based on the original idea of SP are presented. The large-scale dynamics are unchanged, but the small-scale model is solved in a reduced spatially periodic domain to save the computation cost following a similar idea applied by one of the authors for aquaplanet simulations. In addition, the time interval of integration of the small-scale model is reduced systematically for the same purpose, which results in a different coupling mechanism between the small- and large-scale models. The new algorithms have been applied to a stringent two-dimensional test suite involving moist convection interacting with shear with regimes ranging from strong free and forced squall lines to dying scattered convection as the shear strength varies. The numerical results are compared with the CRM and original SP. It is shown here that for all of the regimes of propagation and dying scattered convection, the large-scale variables such as horizontal velocity and specific humidity are captured in a statistically accurate way (pattern correlations above 0.75) based on space–time reduction of the small-scale models by a factor of  $1/3$ ; thus, the new efficient algorithms for SP result in a gain of roughly a factor of 10 in efficiency while retaining a statistical accuracy on the large-scale variables. Even the models with  $1/6$  reduction in space–time with a gain of 36 in efficiency are able to distinguish between propagating squall lines and dying scattered convection with a pattern correlation above 0.6 for horizontal velocity and specific humidity. These encouraging results suggest the possibility of using these efficient new algorithms for limited-area mesoscale ensemble forecasting.

### 1. Introduction

Atmospheric processes of weather and climate cover about 10 decades of spatial scales, from a fraction of a millimeter to planetary. Regarding atmospheric fluid dynamics, one is primarily concerned with spatial scales larger than tens of meters because the smaller scales fall within the inertial range of atmospheric turbulence. Spatial scales between 100 m and 100 km, referred to as small through

mesoscale, show an abundance of processes associated with dry and moist convection, clouds, waves, boundary layer, topographic, and frontal circulations. A major stumbling block in the accurate prediction of weather and short-term climate is the accurate parameterization of moist convection. Cloud-system-resolving models (CRMs) realistically represent small-scale and mesoscale processes. But because of their high computational cost, they cannot be applied to large ensemble-size level weather prediction or climate simulations within the near future.

A different modeling approach, the cloud-resolving convection parameterization (CRCP) or superparameterization (SP) was developed recently (Grabowski and Smolarkiewicz 1999; Grabowski 2001, 2004; Randall et al. 2003). The idea is to use a 2D CRM in each column of a large-scale model to explicitly represent small-scale

---

\* The National Center for Atmospheric Research is sponsored by the National Science Foundation.

---

Corresponding author address: Yulong Xing, Courant Institute of Mathematical Sciences, New York, NY 10012.  
E-mail: xing@cims.nyu.edu

and mesoscale processes and interactions among them. It blends conventional parameterization on a coarse mesh with detailed CRM on a finer mesh. This approach has been shown to be ideal for parallel computations and it can easily be implemented on supercomputers. The method has yielded promising new results regarding tropical intraseasonal behavior (Grabowski 2001, 2004; Khairoutdinov et al. 2005) and has the potential for many other applications in climate–atmosphere–ocean science (Wyant et al. 2006; Majda 2007).

There is a crucial difference in applying SP in a climate model (grid length of a few hundreds of kilometers) and in a limited-area mesoscale (LAM) model (grid length of a few tens of kilometers). The key point is that in the former case both convective and mesoscale dynamics have to be treated by 2D CRM, but only convective dynamics have to be treated by the SP model in the latter (Grabowski 2006). This has far-reaching implications. An obvious one is that the outer model time step is much shorter in the case of the LAM model (a couple of minutes) than in the climate model (tens of minutes). This is important because a time step of a few minutes is significantly shorter than the lifetime of a single convective cell [typically quoted as 20 min; (Byers and Braham 1949)]. This is not the case for the climate model. A similar argument can be made for the size of the domain of the SP model. In the climate model case, the fact that SP has to treat mesoscale dynamics implies that the domain cannot be too small. But for the convective scale only as in the LAM case, it might be possible that the domain can be as small as to host just a single chaotic convective cell.

The purpose of this paper is to present new efficient sparse space–time algorithms for superparameterization (SSTSP), which require less computational cost and yet provide statistically accurate large-scale features. We note that the small-scale models are actually solved over the whole time in the original superparameterization, which occupies the most computational time. In the new efficient algorithm, we can solve the small-scale models for a reduced partial time and over a reduced periodic domain. The reduction in the spatial periodic domain follows the original idea of superparameterization and an application for aquaplanet simulations Grabowski (2002), although the effect of spatial reduction has not been tested systematically before in the present mesoscale context (Grabowski 2006; Majda and Grote 2009). The reduced time strategy is completely novel here. Numerical comparison with a CRM and the original superparameterization shows that the large-scale features are captured in a statistically accurate way. So this reduced approach already contains most of the necessary information needed for the large-scale models. Hence, the computational cost can be reduced significantly. The

paper is organized in the following way. In section 2, the original superparameterization is introduced first, followed by the development of the new efficient algorithms. We test these algorithms on free and forced squall-line simulations, as well as dying scattered convection and compare the numerical results in section 3. Concluding remarks are given in section 4.

## 2. Sparse space–time algorithms for superparameterization

In this section, we start with a brief introduction to the superparameterization approach proposed by Grabowski and Smolarkiewicz (1999) and Grabowski (2001, 2004). By replacing the 3D cloud-scale model by a 2D version, this approach saves the computational cost tremendously, and numerical comparison between SP and CRM simulations shows that this approach captures the large-scale features very well in some situations. We will present a new algorithm based on this approach, by a reduced time strategy, to efficiently solve the models. A reduced space strategy is also presented. Then the combination algorithm based on these two strategies, which will save the computational cost by a factor of  $1/p^2$  for an arbitrary constant  $p$ , is developed.

The strategy underlying the superparameterization approach on mesoscales is to consider two distinct models coupled in a particular way. The first is a 3D large-scale flow model (e.g., a LAM or a GCM). The large-scale model uses a horizontal grid length of a few hundreds of kilometers in a GCM case and a few tens of kilometers in a LAM case (32 km in section 3). The second model is a 2D cloud-scale model formulated on the  $x$ – $z$  plane aligned east–west and embedded in each column of the large-scale model. Cloud-scale and large-scale models use the same vertical grid. The cloud-scale model is applied on a sufficiently fine horizontal grid (1 km) in order to permit moist convective dynamics. The cloud-scale model is periodic in the horizontal.

The large-scale model employs moist anelastic equations. The anelastic system of equations can be compactly written as

$$\begin{aligned} \frac{D\mathbf{U}}{Dt} &= -\nabla\Pi + \mathbf{k}gB + \mathbf{i}F_{CS}^{\mathbf{U}}, & \nabla \cdot (\rho_0 \mathbf{U}) &= 0, \\ \frac{D\Theta}{Dt} &= F_{CS}^{\Theta}, & \frac{DQ_v}{Dt} &= F_{CS}^{Q_v}, & \frac{DQ_c}{Dt} &= F_{CS}^{Q_c}, & \text{and} \\ \frac{DQ_p}{Dt} &= F_{CS}^{Q_p}. \end{aligned} \quad (1)$$

In (1),  $\mathbf{U} = (U, V, W)$  is the large-scale flow in the east–west, north–south, and vertical direction, respectively;  $\Theta$  is the potential temperature; and  $Q_v$ ,  $Q_c$ , and  $Q_p$  are mixing ratios for water vapor, cloud condensate (i.e., condensed water carried by the flow), and precipitation (condensed

water that falls relative to the air), respectively. Here  $D/Dt = \partial/\partial t + \mathbf{U} \cdot \nabla$ ;  $\Pi$  is the pressure perturbation with respect to a balanced ambient state, normalized by the anelastic reference density  $\rho_0$ . The buoyancy  $B = (\Theta - \Theta_e)/\Theta_0 + \epsilon(Q_v - Q_{ve}) - Q_c - Q_p$ , where  $\Theta_e$  and  $Q_{ve}$  are ambient potential temperature and temperature profile,

respectively;  $\Theta_0$  is the reference potential temperature profile; and  $\epsilon + 1$  is the ratio of gas constants of water vapor and dry air. The  $F_{CS}$  terms on the right-hand side of (1) represent the cloud-scale model feedback.

The anelastic equations of the cloud-scale model are as follows:

$$\begin{aligned} \frac{d\mathbf{u}}{dt} &= -\nabla' \pi + \mathbf{k}gb + \mathbf{i}(s_{\mathbf{u}} + f_{LS}^{\mathbf{u}}), \quad \nabla' \cdot (\rho_0 \mathbf{u}) = 0, \quad \frac{d\theta}{dt} = \frac{\theta_e}{T_e} \left[ \frac{L_v}{c_p} (\text{CON} + \text{DEP}) + r \right] + s_{\theta} + f_{LS}^{\theta}, \\ \frac{dq_v}{dt} &= -\text{CON} - \text{DEP} + s_{q_v} + f_{LS}^{q_v}, \quad \frac{dq_c}{dt} = \text{CON} - \text{ACC} - \text{AUT} + f_{LS}^{q_c}, \quad \text{and} \\ \frac{dq_p}{dt} &= \frac{1}{\rho_0} \frac{\partial}{\partial z} (\rho_0 v_t q_p) + \text{ACC} + \text{AUT} + \text{DEP} + f_{LS}^{q_p}, \end{aligned} \quad (2)$$

where the lowercase symbols have the same meaning as the respective uppercase symbols in (1). Here  $d/dt \equiv \partial/\partial t + \mathbf{u} \cdot \nabla'$  with  $\nabla' \equiv (\partial/\partial x, \partial/\partial z)$ . The terms  $f_{LS}$  represent the large-scale forcing for the cloud-scale model;  $L_v$  and  $c_p$  are the latent heat of condensation and the specific heat at constant pressure; and  $\theta_e$  and  $T_e$  are the environmental potential temperature and temperature profiles, respectively. The sources on the right-hand side of (2) describe the formation of cloud condensate from water vapor (CON), autoconversion of cloud condensate into precipitation (AUT), accretion of cloud condensate by precipitation (ACC), and source/sink of precipitation due to deposition/evaporation of water vapor on/from precipitation particles (DEP). These sources are represented using the simple scheme of Grabowski (1998).

We denote the large-scale variables by  $Q$  (representing a collection of  $\mathbf{U}$ ,  $\Theta$ , and  $Q_v$ , etc.), and small-scale variables by  $q$ . The coupling formalism of the large-scale and cloud-scale models is through the terms  $f_{LS}$  and  $F_{CS}$ .

In the original superparameterization implementation, the large-scale models are solved from  $T$  to  $T + \Delta T$  in the following way (Grabowski 2004):

$$Q|^{n+1} = Q|^{n+1} + \Delta T(A_Q + S_Q)|_n^{n+1} + \Delta T F_{CS}^Q|_n^n, \quad (3)$$

where  $A_Q \equiv -\mathbf{U} \cdot \nabla Q$  is the large-scale advection term ( $\mathbf{U}$  is the large-scale flow),  $S_Q$  is the large-scale sources [pressure gradient or Coriolis acceleration in (1), etc.],  $F_{CS}^Q$  is the source due to small-scale processes, referred as the small-scale feedback, and the notation  $|_n^{n+1}$  means numerical time average of these terms. The large-scale forcing to the small-scale models is defined as

$$f_{LS}^q|_n^n = \frac{Q|^{n+1} - \langle q|_n^n \rangle}{\Delta T}, \quad (4)$$

where  $\langle \rangle$  represents the spatial average over the small-scale domain. The small-scale models are solved from  $T$  to  $T + N\Delta t$  ( $\Delta T = N\Delta t$  is assumed) by

$$q|^{n+1} = q|^{n+1} + \sum_{i=1}^N \Delta t (a_q + s_q)|_i^{i+1} + \sum_{i=1}^N \Delta t f_{LS}^q|_i^n, \quad (5)$$

where  $a_q \equiv -\mathbf{u} \cdot \nabla q$  ( $\mathbf{u}$  is the small-scale flow),  $s_q$  represents small-scale sources (surface drag for velocity or latent heating due to phase changes, etc.). Note that although the small-scale models are solved for  $N$  steps within the big time step  $\Delta T$ , the same large-scale forcing  $f_{LS}^q|_i^n$  is employed. Finally, the small-scale feedback is defined by

$$F_{CS}^Q|_n^{n+1} = \frac{\langle q|^{n+1} \rangle - Q|^{n+1}}{\Delta T}. \quad (6)$$

*a. Reduced time strategy*

In the implementation above,  $\Delta T = N\Delta t$  is assumed, so that the small-scale models are actually solved over the whole time, which brings a high computational cost. As we notice from the strategy explained above, all we need from the small-scale models is the small-scale feedback in (6). We can solve the small-scale models for part of the time interval and find an approximate estimation of  $F_{CS}^Q|_n^{n+1}$ . It may contain all the necessary statistical information needed for the large-scale model.

Thus, we want to save computational cost by using  $N/p$  small-scale time steps instead of  $N$  small-scale time steps, for an arbitrary constant  $p$ . So we follow the same strategy, and solve the large-scale models first by (3). Because the small-scale models are solved from  $T$  to  $T + N/p\Delta t = T + \Delta T/p$ , we define the new large-scale forcing as

$$f_{\text{LS}}^q|^n = \frac{Q|^n - \langle q|^n \rangle}{\Delta T/p} = p \frac{Q|^n - \langle q|^n \rangle}{\Delta T}, \quad (7)$$

where  $\Delta T/p$  is used instead of  $\Delta T$  as in (4). Then the solver for the small-scale models takes the following form:

$$q|^{n+(1/p)} = q|^n + \sum_{i=1}^{N/p} \Delta t (a_q + s_q)|_i^{i+1} + \sum_{i=1}^{N/p} \Delta t f_{\text{LS}}^q|^n. \quad (8)$$

The last term  $\sum_{i=1}^{N/p} \Delta t f_{\text{LS}}^q|^n$  represents the forcing of the large-scale model to the small-scale models, and we have the relation

$$\begin{aligned} \sum_{i=1}^{N/p} \Delta t f_{\text{LS}}^q|^n &= \frac{N}{p} \Delta t p \frac{Q|^n - \langle q|^n \rangle}{\Delta T} \\ &= \sum_{i=1}^N \Delta t \frac{Q|^n - \langle q|^n \rangle}{\Delta T}, \end{aligned} \quad (9)$$

where the right-hand side is exactly the last term of (5) in the original superparameterization approach. Hence, although the small-scale models are solved in a reduced time interval, the impact of the large-scale models on small-scale models are fully resolved through the approach above. We anticipate that this approach can capture the large-scale variables reasonably well under appropriate circumstances.

Next we need to obtain  $q|^{n+1}$ , which is necessary for the large-scale model. The simple assumption  $q|^{n+1} = q|^{n+1/p}$  is employed here (see section 2d for an interpretation). Finally, we define the small-scale feedback as the same formula from (6):

$$F_{\text{CS}}^Q|^n = \frac{\langle q|^{n+1} \rangle - Q|^n}{\Delta T} = \frac{\langle q|^{n+1/p} \rangle - Q|^n}{\Delta T}. \quad (10)$$

In summary, the change is to multiply the original large-scale forcing by  $p$  and keep the same small-scale feedback. By doing this, the small-scale models are solved from  $T$  to  $T + N/p\Delta t$ , and we reduce the computational cost by a factor of  $1/p$ .

### b. Reduced space strategy

In the previous section, we considered the case to use  $1/p$  small-scale time steps to save the computational cost. Following this direction, here we consider a similar possible spatial strategy (i.e., using  $1/p$  small-scale spatial cells for an arbitrary constant  $p$ ). To be simple, we assume the large-scale model is two-dimensional, but the whole strategy introduced here can be easily implemented into 3D large-scale/2D small-scale models without any change.

In the original mesoscale superparameterization (Grabowski 2006), the large-scale domain is divided into grids with horizontal size  $\Delta X$  of a few tens of kilometers, which is also assigned to be the domain of each small-scale simulation. Here, we keep the large-scale cell size be  $\Delta X$ , but let the horizontal domain of the small-scale models be  $\Delta X/p$ . By doing this, we do not need to solve the small-scale model everywhere. However, optimistically, the reduced model can capture enough small-scale effects statistically, and pass them to the large-scale model correctly. We mention again that the contribution of the small-scale models to the large-scale models is through the small-scale feedback  $F_{\text{CS}}^Q$ . A similar idea has been applied by one of the authors for aquaplanet simulations Grabowski (2002) in the original superparameterization.

The large-scale forcing and small-scale feedback remain the same, but the spatial average is over the smaller  $\Delta X/p$  periodic domain:

$$\begin{aligned} f_{\text{LS}}^q|^n &= \frac{Q|^n - \langle q|^n \rangle}{\Delta T} \quad \text{and} \\ F_{\text{CS}}^Q|^n &= \frac{\langle q|^{n+1} \rangle - Q|^n}{\Delta T}. \end{aligned} \quad (11)$$

Everything else is the same: the models are solved by (3) and (5).

### c. Reduced time and space together

In the preceding discussion, we first introduced how to save the computational cost by reducing the time interval of integration by the small-scale model, then we showed how similar spatial savings can be obtained. It is natural to combine those two strategies to save both time and spatial computational cost. Assume  $1/p$  small-scale time steps and spatial cells are both employed, then the savings are large, since the computational cost is decreased by  $1/p^2$ .

Although the combination of these is rather straightforward, we summarize and present the new efficient SSTSP below:

- Solve the large-scale models first by

$$Q|^{n+1} = Q|^n + \Delta T (A_Q + S_Q)|_n^{n+1} + \Delta T F_{\text{CS}}^Q|^n. \quad (12)$$

- Define the new large-scale forcing, with the spatial average over the  $\Delta X/p$  domain:

$$f_{\text{LS}}^q|^n = \frac{Q|^n - \langle q|^n \rangle}{\Delta T/p} = p \frac{Q|^n - \langle q|^n \rangle}{\Delta T}. \quad (13)$$

- Solve the small-scale models by

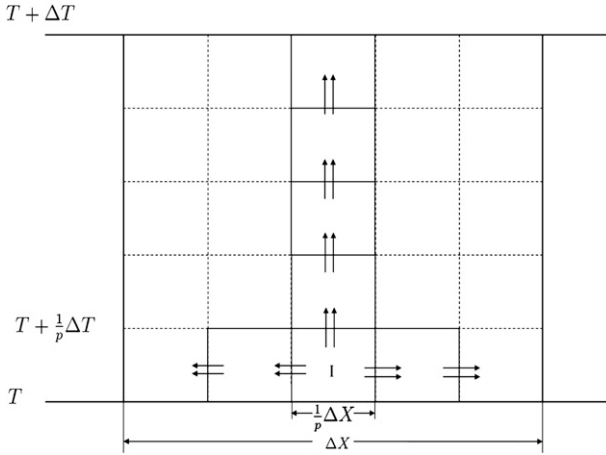


FIG. 1. Periodic extension of the small-scale solution on the small domain I to the big domain. An illustration of  $p = 5$ .

$$|q|^{n+1/p} = |q|^n + \sum_{i=1}^{N/p} \Delta t (a_q + s_q)_i^{i+1} + \sum_{i=1}^{N/p} \Delta t f_{LS}^q |q|^n. \quad (14)$$

- Assume  $|q|^{n+1} = |q|^{n+1/p}$ , and define the small-scale feedback as

$$F_{CS}^Q |q|^{n+1} = \frac{\langle |q|^{n+1} \rangle - Q |q|^{n+1}}{\Delta T} = \frac{\langle |q|^{n+1/p} \rangle - Q |q|^{n+1}}{\Delta T}, \quad (15)$$

- with the spatial average over  $\Delta X/p$  domain.

Note that the space-reducing parameter and the time-reducing parameter are set equal here for convenience, but this is not essential.

*d. An alternative formulation of the algorithm*

In each time step of the original SP and SSTSP, we solve the large-scale models first, and then the small-scale models. We can switch the order and obtain an alternative formulation with an interesting reinterpretation of the method.

For SP, we can first solve the small-scale models from  $T$  to  $T + N\Delta t = T + \Delta T$  by

$$\begin{aligned} \langle |q|^{n+1} \rangle &= \langle |q|^n \rangle + \sum_{i=1}^N \Delta t \langle (a_q + s_q)_i^{i+1} \rangle \\ &+ \sum_{i=1}^N \Delta t \langle f_{LS,SO}^q |q|^n \rangle, \end{aligned} \quad (16)$$

where  $f_{LS,SO}^q$  is the large-scale forcing for the small-scale models with ‘‘SO’’ representing ‘‘switching order.’’ The small-scale feedback to the large-scale models is then defined as

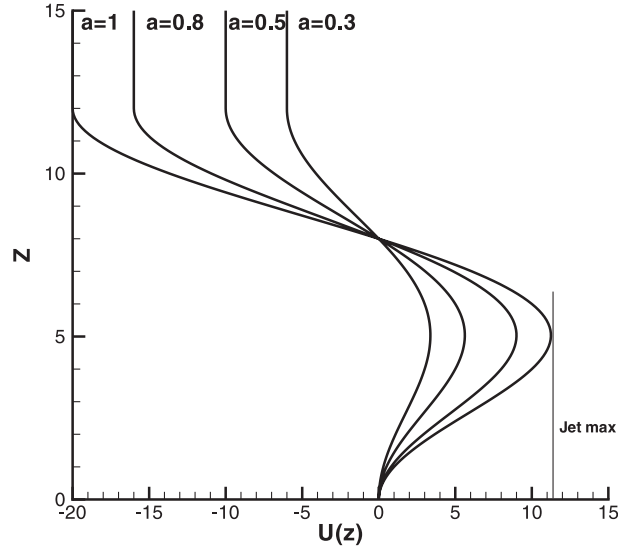


FIG. 2. Plot of  $\bar{U}(z)$ .

$$F_{CS,SO}^Q |q|^n = \frac{\langle |q|^{n+1} \rangle - Q |q|^n}{\Delta T}. \quad (17)$$

With these data, the large-scale models are then solved from  $T$  to  $T + \Delta T$  by

$$Q |q|^{n+1} = Q |q|^n + \Delta T (A_Q + S_Q) |q|^{n+1} + \Delta T F_{CS,SO}^Q |q|^n, \quad (18)$$

and the large-scale forcing to small-scale models is set as

$$f_{LS,SO}^q |q|^{n+1} = \frac{Q |q|^{n+1} - \langle |q|^{n+1} \rangle}{\Delta T}. \quad (19)$$

Note that a different form of large-scale forcing and small-scale feedback are obtained because of this switch. Simple calculation leads to the following relation:

$$\begin{aligned} Q |q|^{n+1} &= Q |q|^n + \Delta T (A_Q + S_Q) |q|^{n+1} \\ &+ \sum_{i=1}^N \Delta t \langle (a_q + s_q)_i^{i+1} \rangle, \end{aligned} \quad (20)$$

which means that large-scale variables include all the required effects at the  $n + 1$  time level. The small-scale variables, on the other hand, do not include the large-scale forcing at the  $n + 1$  time level. Note that for the original SP (Grabowski 2004), the situation is reversed and the small-scale model has all the sources correct:

$$\begin{aligned} \langle |q|^{n+1} \rangle &= \langle |q|^n \rangle + \Delta T (A_Q + S_Q) |q|^{n+1} \\ &+ \sum_{i=1}^N \Delta t \langle (a_q + s_q)_i^{i+1} \rangle, \end{aligned} \quad (21)$$

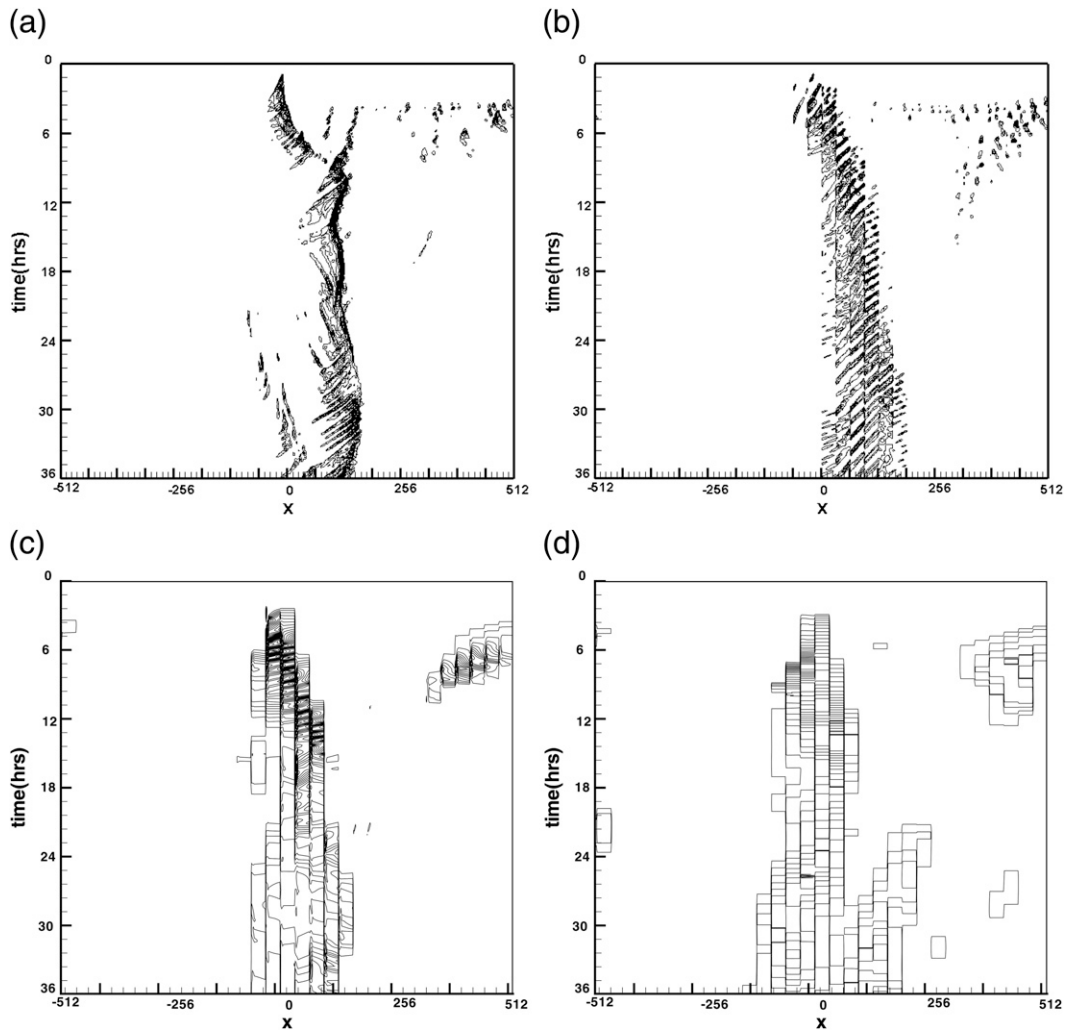


FIG. 3. The contours of the surface precipitation from different simulations when  $a = 1$ : (a) CRM squall-line simulation, (b) SP, (c) SSTSP3, and (d) SSTSP6.

and the large-scale model does not include the small-scale feedback at the  $n + 1$  time level.

The same thing can be applied on the SSTSP algorithms. We first solve the small-scale models by

$$\begin{aligned} \langle q^{n+1/p} \rangle &= \langle q^n \rangle + \sum_{i=1}^{N/p} \Delta t \langle (a_q + s_q)_i^{i+1} \rangle \\ &+ \sum_{i=1}^{N/p} \Delta t \langle f_{\text{LS,os}}^q |^n \rangle, \end{aligned} \quad (22)$$

with the spatial average over  $\Delta X/p$  domain. By assuming  $q^{n+1} = q^{n+1/p}$ , we define the small-scale feedback as

$$F_{\text{CS,os}}^Q |^n = \frac{\langle q^{n+1/p} \rangle - Q^n}{\Delta T/p} = p \frac{\langle q^{n+1} \rangle - Q^n}{\Delta T}. \quad (23)$$

The large-scale models are then solved by

$$Q^{n+1} = Q^n + \Delta T (A_Q + S_Q) |_{n+1}^{n+1} + \Delta T F_{\text{CS,os}}^Q |^n, \quad (24)$$

and the large-scale forcing is

$$f_{\text{LS,os}}^q |^{n+1} = \frac{Q^{n+1} - \langle q^{n+1} \rangle}{\Delta T}. \quad (25)$$

The two main changes, when compared with SP, include the same assumption  $q^{n+1} = q^{n+1/p}$  utilized earlier in section 2c, and also that the small-scale feedback  $F_{\text{CS,os}}^Q |^n$  is  $p$  times bigger, which can both be explained in the following way. Instead of solving the small-scale models in the original  $\Delta X \times \Delta T$  domain denoted by  $D$ , we limit them to a much smaller domain  $1/p \Delta X \times 1/p \Delta T$  in SSTSP, denoted by  $I$  in Fig. 1. We can periodically extend the solutions in space-time inside the domain  $I$ , to

TABLE 1. The jet max and squall-line speed of these five simulations when  $a = 1$ .

	CRM	SP	SSTSP2	SSTSP3	SSTSP6
Jet max (km)	11.25	11.25	11.25	11.25	11.25
Mean propagation speed (m s <sup>-1</sup> )	8.25	8.25	8.25	8.25	8.25

the big domain  $D$ , as shown in Fig. 1. Then we obtain an approximate solution of the small-scale model everywhere inside the domain  $D$ . The assumption  $q|^{n+1} = q|^{n+1/p}$ , used here and in the earlier SSTSP algorithm, can be easily understood following this periodic extension. From time  $T$  to  $T + \Delta T$ , small-scale models solutions on domain  $I$  are repeated  $p$  times. Therefore, the small-scale feedback, which represents the information transferred from small-scale models to large-scale models during time interval  $[T, T + \Delta T]$ , should be  $p$  times the one contributed by the small domain  $I$  only. This explains the two main changes between SP and SSTSP methods, as pointed out above. To be consistent with the original SP developed by Grabowski (2004), the performance of the SSTSP algorithms developed in section 2c will be assessed on a stringent test bed in section 3. However, the alternative algorithm developed here with this appealing interpretation has also been tested and performs comparably on the same stringent test bed. The correlations differ in the third decimal place.

### 3. Application to squall lines

In this section, we apply the new efficient sparse space–time algorithms developed in section 2 to squall-

line experiments that have either dying scattered convection or quasi-steady squall lines of varying strength for a long time. We also run the same tests with a CRM simulation and the original SP approach. The comparison of these numerical results shows that significant large-scale features such as horizontal velocity and specific humidity are captured with significant skill by the new SSTSP algorithms as well as the mean propagation speed. Furthermore, the regime of dying scattered convection with weak ambient shear is also captured by the SSTSP algorithms. The standard units kilometers (for  $x$  and height  $z$ ) and meters per second (for velocity) will be used in the following sections without further explanation.

#### a. Experimental design

We explore the squall-line experiment designed in Jung and Arakawa (2005) and Grabowski (2006) to test the superparameterization algorithm. A similar suite of experiments are developed in Majda and Xing (2010) to analyze the multiscale properties of squall lines. The model we solve is a simplified 2D version of (1) and (2) in both the large-scale and small-scale models. Horizontal velocities  $\mathbf{U}_h$  and  $\mathbf{u}_h$  are reduced to the east–west component only. The large-scale model has a 2D domain of 1024-km length and 25-km height, with the horizontal grid size 32 km. The CRM is run on this domain with 1-km resolution and provides the truth standard to test performance of the SSTSP algorithms. We also run mesoscale SP as in Grabowski (2006) with full spatial resolution in order to explore the effect of the spatial periodicity approximation alone. Thus, for the superparameterization test, the small-scale model is solved on each cell, hence the periodic domain is 32 km long and

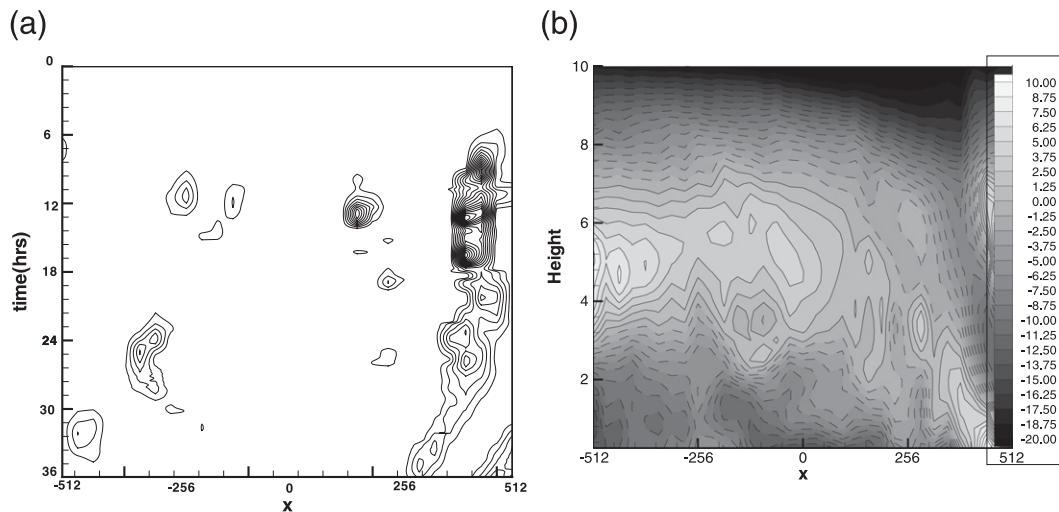


FIG. 4. The contours from the CRM test with 32-km resolution when  $a = 1$ : (a) surface precipitation and (b) large-scale horizontal velocity.

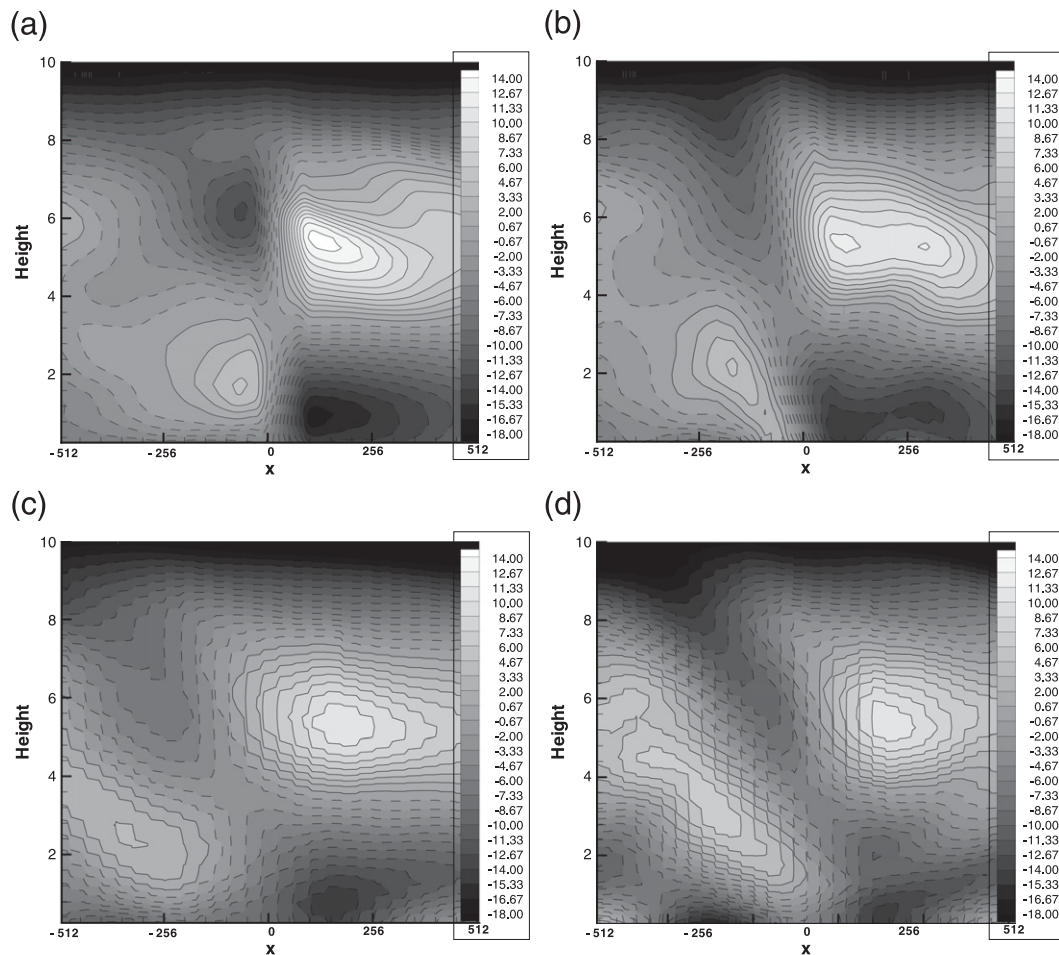


FIG. 5. The contours of the large-scale horizontal velocity  $\langle \bar{u} \rangle$  from different simulations when  $a = 1$ : (a) CRM squall-line simulation, (b) SP, (c) SSTSP3, and (d) SSTSP6.

25 km high. A total of 32 independent small-scale models are solved through the 1024-km horizontal domain. A uniform 1-km horizontal grid is used for the small-scale models as in the CRM. A 100-point vertical grid is taken for both large- and small-scale models, with a gravity wave absorber applied in the uppermost 7 km of the domain. The time step is set as 60 s for the large-scale models, and 10 s for the small-scale models, hence the small-scale models are solved 6 times in each big time step. An open lateral boundary condition is utilized for the large-scale model, and a periodic boundary condition is used for the small-scale model. The initial temperature, humidity profiles and horizontal wind fields are based on the Global Atmospheric Research Program (GARP) Atlantic Tropical Experiment (GATE) phase-III mean sounding. In standard fashion, a 4-km-deep, 512-km-long cold pool of  $D\theta' = -6.75$  K and  $Dq'_v = -3.5$  g kg<sup>-1</sup> (see Majda and Xing 2010 for details) is placed in the domain on the initial data to initiate convection. This initial cold

pool is set to mimic the background cold air produced by a decaying cold front in the synoptic environment.

A large-scale forcing representing the climatological background is imposed on the model through the cooling and moistening rates. We keep this large-scale forcing for 6 h, then remove it and observe whether a squall line forms and keeps propagating for many hours afterward as a turbulent free-traveling wave. To provide small-scale excitation (important for the initial development of convection), a 10% amplitude random noise is added to the surface fluxes, with random numbers generated at every model time step. Rotational effects are not considered.

#### THE TEST BED

We use a stringent test bed to evaluate the computational performance of the SSTSP algorithms. Four different initial large-scale background shears are used to generate the squall lines. They are given by

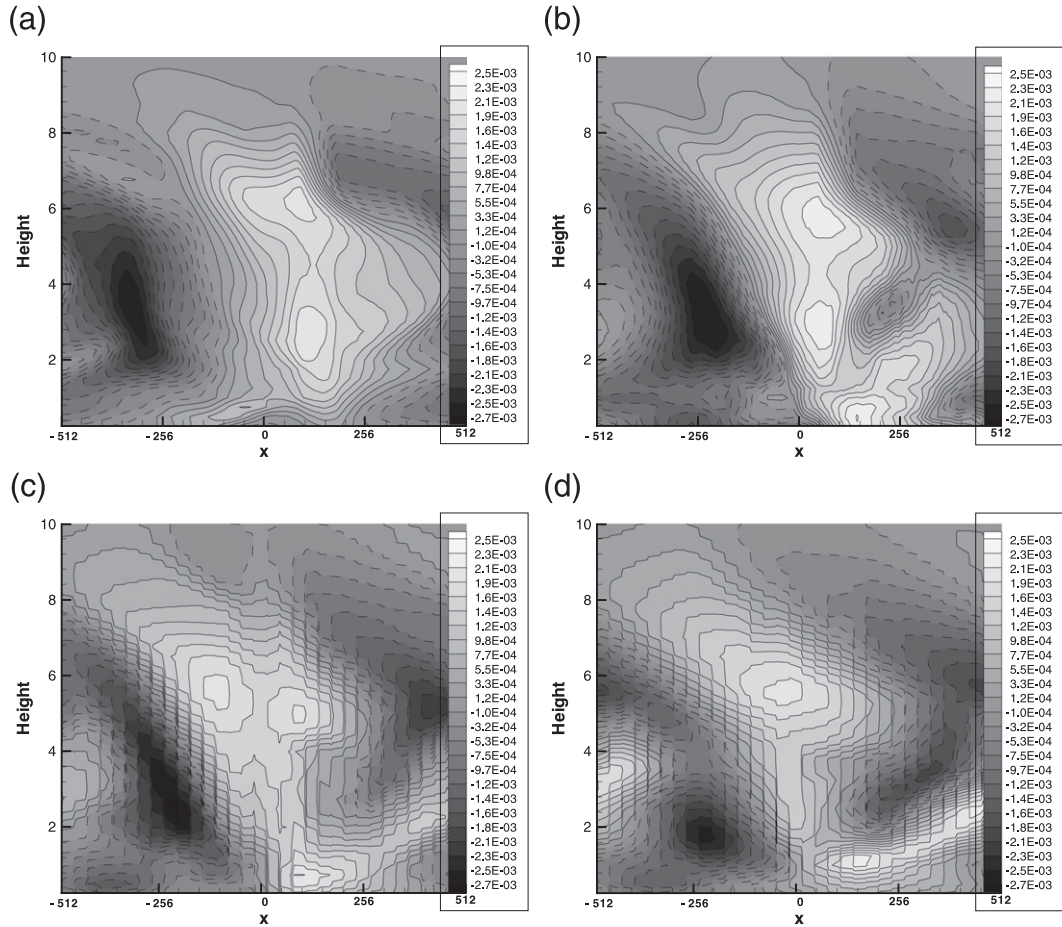


FIG. 6. As in Fig. 5, but for the contours of the large-scale specific humidity ( $\bar{q}_v$ ) from different simulations when  $a = 1$ .

$$\bar{U}(z) = \begin{cases} 10a \left[ \cos\left(\frac{\pi z}{12}\right) - \cos\left(\frac{2\pi z}{12}\right) \right], & \text{if } z < 12, \\ -20a, & \text{otherwise,} \end{cases} \quad (26)$$

for a fixed coefficient  $a$ . We show the case when  $a = 1$  in Fig. 2. The jet max refers to the maximum of the background shear, which is marked in Fig. 2. Next, we run this squall-line experiment for four different cases with  $a = 1$  (a strong background shear),  $a = 0.8$  (a weak shear), and  $a = 0.5$  (a weaker shear), as well as  $a = 0.3$ . We systematically reduce the ambient shear and thus raise the Richardson number (Majda 2003, chapter 3). Thus, the resulting forcing strength implied by the method changes quite a lot from experiment to experiment for large values of  $p$ . This is achieved in the test bed. It is shown that a propagating squall line always emerges in these three cases with the same speed (Majda and Xing 2010). The weakest shear,  $a = 0.3$ , results in dying scattered convection. We repeat these tests with the SSTSP algorithms and want the coarse numerical

methods to reproduce this behavior. If the squall line has zero propagation speed in a reference frame, it is easier to process statistical data. For this purpose, in standard fashion, we subtract the mean propagation speed, which can be obtained by calculating the propagation speed of the surface precipitation, from the initial large-scale vertical wind profile in our experiment so the squall line stays near the center of the domain. This is the background shear we actually use and get statistically steady turbulent fronts. In addition, in section 3d, we consider forced propagating squall lines to compare the speed of propagation predicted by SSTSP in an inhomogeneous environment.

TABLE 2. The correlation between the large-scale variables [defined in (27)] from these simulations for  $a = 1$ .

		SP	SSTSP2	SSTSP3	SSTSP6
$\langle \bar{u} \rangle$	SP	—	0.9025	0.8621	0.5876
	CRM	0.9132	0.8735	0.8082	0.6215
$\langle \bar{q}_v \rangle$	SP	—	0.9417	0.8738	0.7168
	CRM	0.8932	0.8521	0.7781	0.6571

### b. Performance of the SSTSP algorithms

In this subsection, we apply the new efficient SSTSP explained in section 2 to the above test bed. Three different simulations are considered with different coefficients  $p$ . To make the comparison, we apply the original SP to the same squall-line experiment, and also the CRM simulation in the same setup. The large-scale features are compared to check the statistical accuracy of the SSTSP algorithms. (Note that by using the efficient algorithms, computational cost is saved by a factor of  $1/p^2$ .) Detailed results are shown.

We start with the case when  $a = 1$  for the background shear in (26). We run the original SP simulation, CRM test, and 3 different SSTSP algorithms with  $p$  (defined in section 2) = 2, 3, and 6, respectively. From now on, we refer to these five simulations as SP, CRM, SSTSP2, SSTSP3, and SSTSP6, with no further explanation. In the

original superparameterization, the small-scale periodic domain size is 32 km and the small-scale models are solved 6 times in each big time step. As mentioned in section 2,  $1/p$  small-scale time steps and  $1/p$  small-scale horizontal cells are used in the efficient algorithms to save the computational cost. Hence, the small-scale periodic domain size is set as 16, 10, and 6 km, respectively, for the SSTSP2, SSTSP3, and SSTSP6, while the small-scale models are solved for 3, 2, and 1 time steps, respectively, in each big time step. The savings in computational cost,  $1/p^2$ , can be easily observed from these reductions.

We run the experiments for 36 h, when the squall line remains statistically steady for a long time. This can be observed from the contour plots of the surface precipitation, as shown in Fig. 3. In Table 1, we show the mean propagation speed (also noted as squall-line speed), and jet max, from which we observe that mean propagation speeds keep the same for all these five experiments.

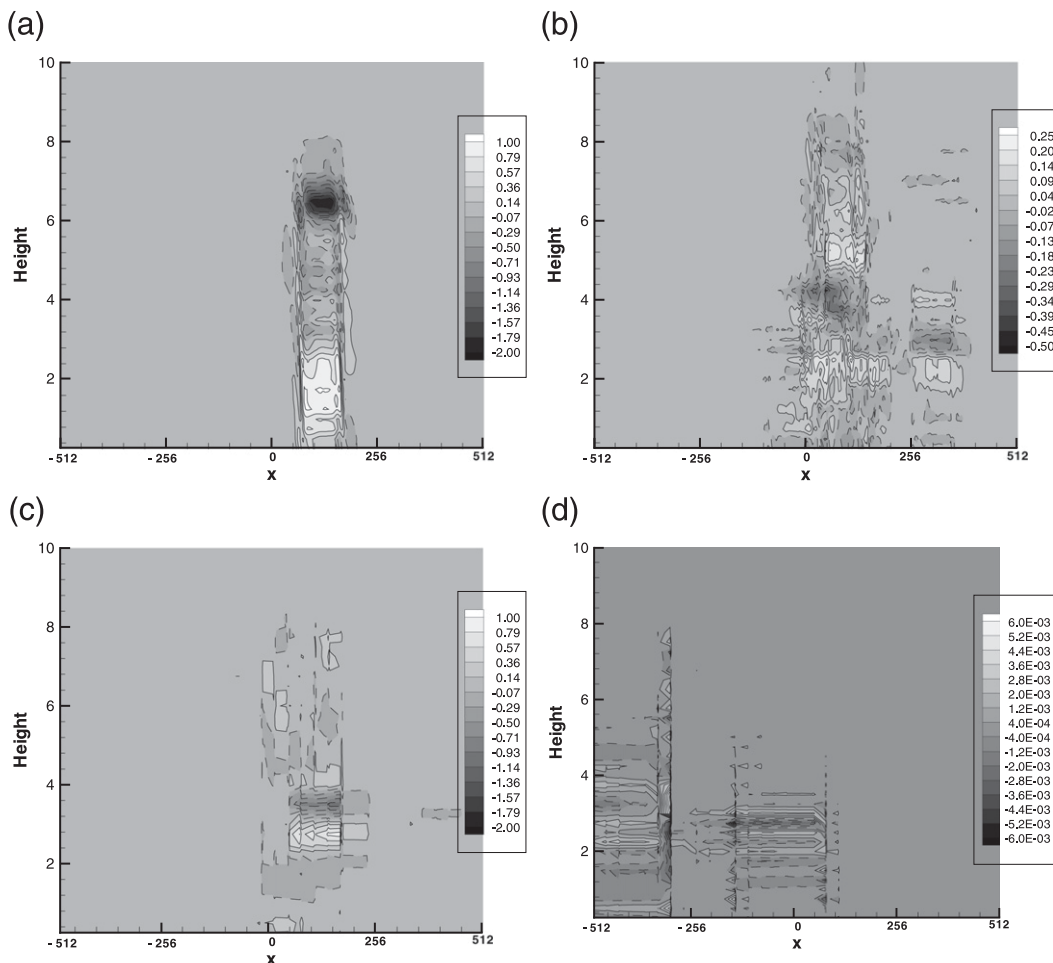


FIG. 7. The contours of the eddy flux  $-\overline{(u'w')_z}$  [ $(\text{m s}^{-1})^2 \text{ km}^{-1}$ ] from different simulations when  $a = 1$ : (a) CRM squall-line simulation, (b) SP, (c) SSTSP3, and (d) SSTSP6. [Note: Different scales are used in this figure. The scale in (d) is much smaller.]

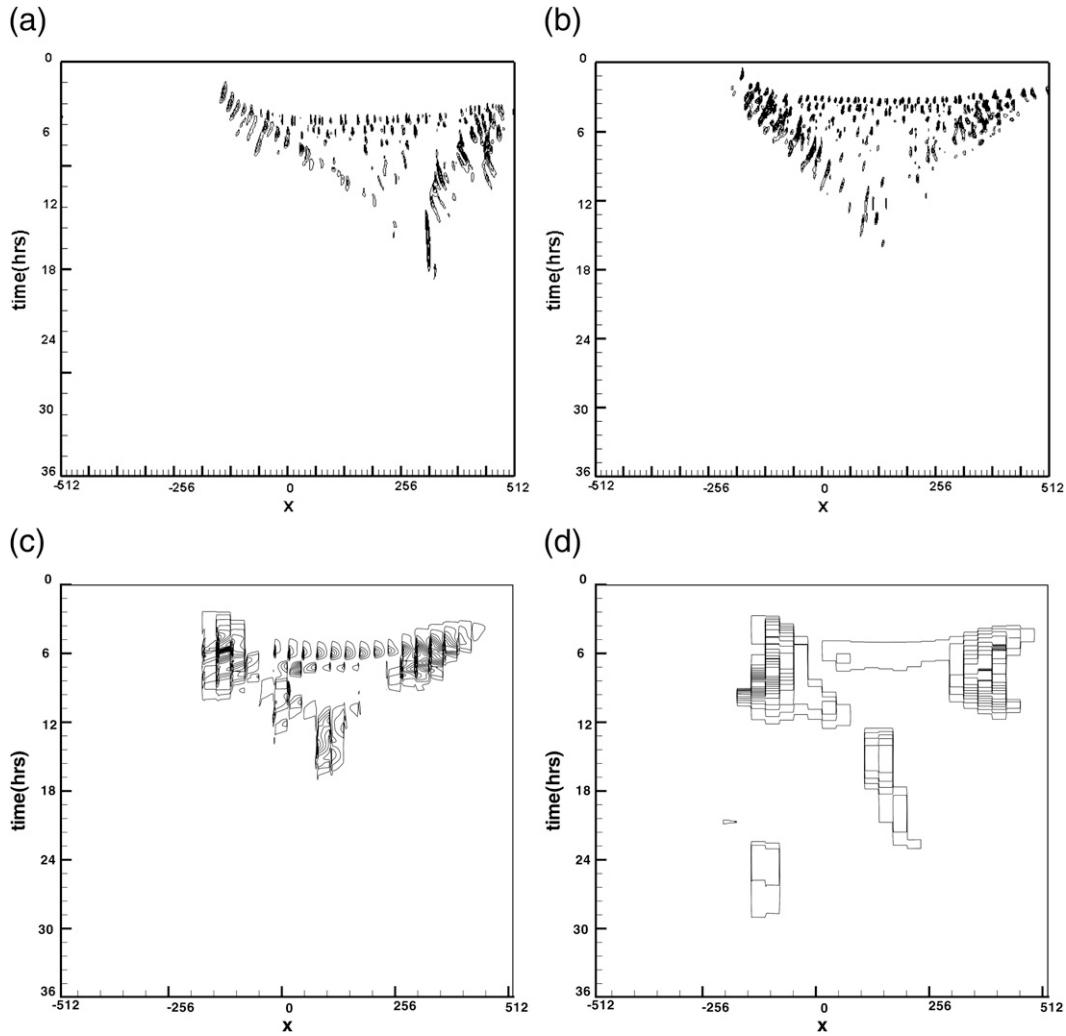


FIG. 8. The contours of the surface precipitations from different simulations with  $a = 0.3$ : (a) CRM squall-line simulation, (b) SP, (c) SSTSP3, and (d) SSTSP6.

These results show that the reduced description through the SSTSP algorithms does not affect the propagation speed of the squall line. One may wonder whether that is because the small-scale models have negligible impact. To emphasize that the small-scale models play an important role in capturing the squall line, we run the CRM code with very coarse 32-km resolution, which is exactly the resolution for the large-scale model of the SP test. The other setup is the same as the above test. The surface precipitation and large-scale horizontal velocity, as defined in (27), are shown in Fig. 4, from which we can observe that no squall line is developed on such coarse meshes. The resolution is too big to capture those cloud-scale effects, while these effects are measured by the small-scale model in the SP and SSTSP tests, and thus information is passed to the large-scale model through the small-scale feedback.

Next, we concentrate on large-scale features in these simulations. As we can see from the surface precipitation contour plots, these squall lines are statistically quasi-steady as turbulent traveling waves after the initial phase. Hence, we compute the time average over the 5 h between the 18th and 23rd hours to gather time-averaged statistical data. This time-averaged numerical solution of horizontal velocity is denoted by  $\langle u \rangle(x)$ . Thus, the large-scale horizontal velocity  $\langle \bar{u} \rangle$ , on mesoscales of order 100 km, is defined as the spatial average:

$$\langle \bar{u} \rangle(x) = \frac{1}{96} \int_{-48}^{48} \langle u \rangle(x + s) ds, \tag{27}$$

and the spatial fluctuation of velocity is given by

$$\langle u' \rangle(x) = \langle u \rangle(x) - \langle \bar{u} \rangle(x). \tag{28}$$

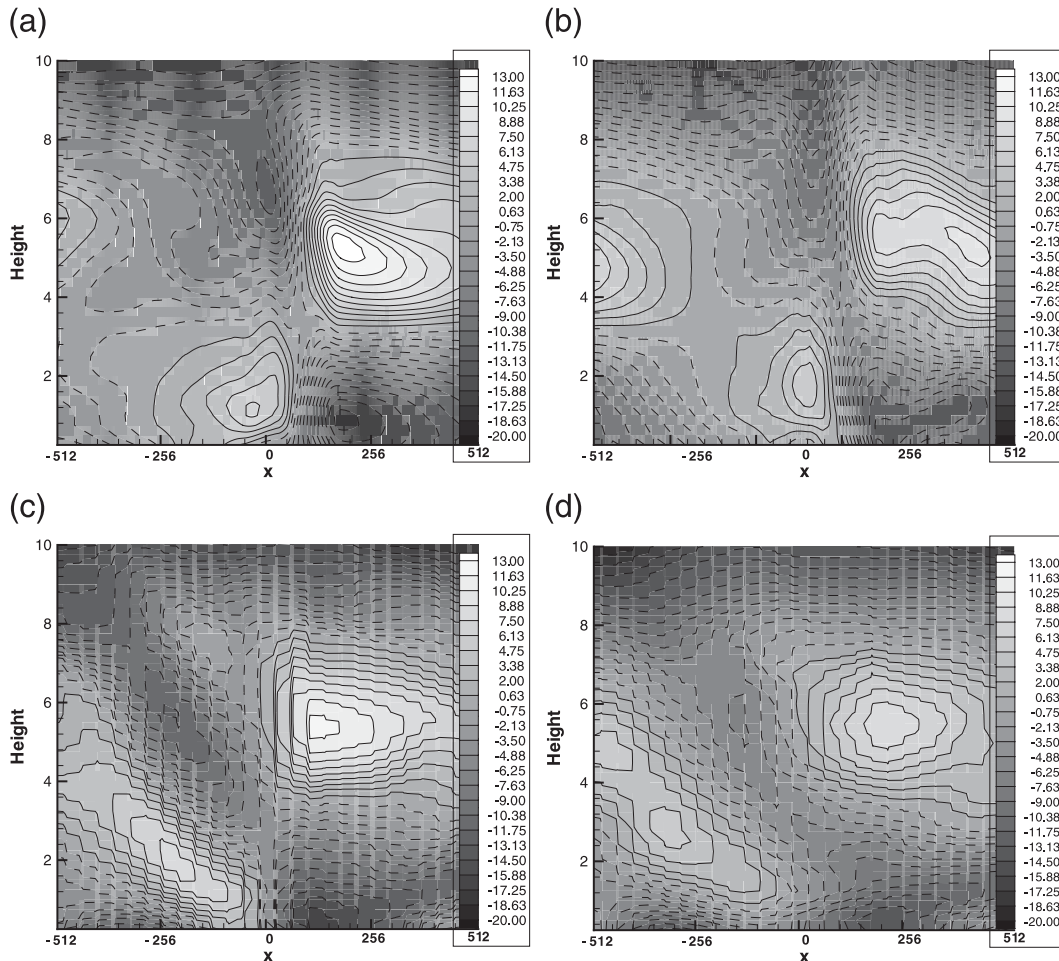


FIG. 9. The contours of the large-scale horizontal velocity  $\langle \bar{u} \rangle$  from different simulations when  $a = 0.8$ : (a) CRM squall-line simulation, (b) SP, (c) SSTSP3, and (d) SSTSP6.

For computational convenience, 96 is used instead of 100 in (27). Similarly, we can compute  $\langle \bar{\theta} \rangle$  and  $\langle \bar{q}_v \rangle$ . The large-scale horizontal velocity and specific humidity are shown in Figs. 5 and 6 for different experiments. From these figures, we observe that the large-scale horizontal velocities have very similar structures, which have shock-like structures with strong negative velocities at low levels in front but at high levels behind the squall line (i.e., a jump updraft; Lafore and Moncrieff 1989). To further explore the statistical skill of the SSTSP algorithms, we compute the correlation between these plots. The results are shown below in Table 2. We remind the reader that these large-scale variables are the most important thing to examine as the output in a squall line. The correlation is above 0.75 for both the horizontal velocity and humidity for the simulations SSTSP2 and SSTSP3, which shows nice structural agreement. Hence, the large-scale variables are captured well in a statistical way by our new efficient algorithms SSTSP2 and SSTSP3, with a much lower com-

putational cost. Even SSTSP6 has pattern correlation above 0.6 for velocity and humidity. There are only six grid points in the small-scale model with SSTSP6; nevertheless, there is enough chaotic dynamics here in the small-scale model to capture some statistical features of the CRM simulation.

As shown in Lafore and Moncrieff (1989), Wu and Moncrieff (1996), and Houze (2004), the eddy flux divergences  $-\langle u'w' \rangle_z$  and  $-\langle w'\theta' \rangle_z$  can be important in determining the large-scale features. Among them, the eddy momentum flux divergence  $-\langle u'w' \rangle_z$  has been shown to be one important connection between the large- and small-scale models. We show  $-\langle (u') \langle w' \rangle \rangle_z$  explicitly in Fig. 7. From the result of the CRM test, we can observe that there exists a positive region below and a negative region above. The positive momentum flux divergence below is associated with the acceleration of the positive large-scale flow and the deceleration of negative flow in these areas, which is a typical example

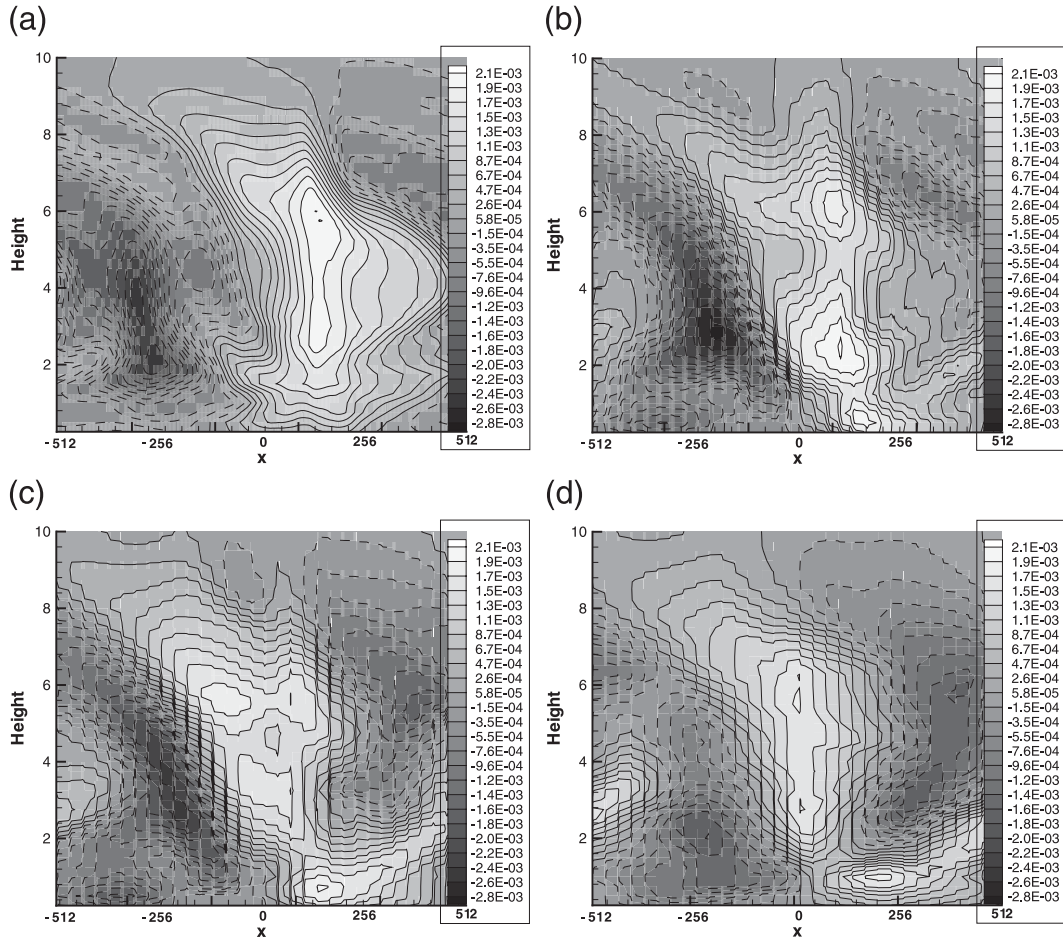


FIG. 10. As in Fig. 9, but for the large-scale specific humidity.

of the upscale transfer in squall lines of moist available potential energy to the large-scale horizontal momentum (Lafore and Moncrieff 1989; Moncrieff 1992; Wu and Moncrieff 1996; Moncrieff and Liu 2006; Majda and Xing 2010). This phenomenon is captured qualitatively by both the SP and the SSTSP3 algorithm, although the detailed vertical location of the dipole structure is different and the magnitude of the eddy flux divergence is diminished. The fact that the full-resolution SP has this vertical discrepancy suggests that the source of this shift in the dipole is the periodic spatial domain in the small-scale models in SP. This shows that SSTSP3 algorithm is a good statistical approximation to the CRM results, but with a gain of a factor of 9 in efficiency over SP. We also find that SSTSP6 does not provide a satisfying result here for this eddy momentum flux divergence.

*c. Numerical results with weaker shears*

In this subsection, we repeat the same numerical tests as in section 3b, but with weaker background shears. Notice that the background shear is defined in (15) with a pa-

rameter  $a$ , which is set as 1 in section 3b. Here we run the same tests with  $a = 0.8$ ,  $a = 0.5$ , and  $a = 0.3$ , respectively. We want to show that SSTSP algorithms capture the large-scale features of the CRM in these tests as well.

As shown in Majda and Xing (2010), we find that when  $a = 0.3$  or smaller, the squall line generated by CRM test dies after the initial formation. We repeat this test for SP, SSTSP2, SSTSP3, and SSTSP6, and the same behavior is observed. The corresponding surface precipitation is shown in Fig. 8 for  $a = 0.3$ , from which we observe that for the first few hours the initial cold pools generate forced squall lines. The squall lines stay there for few hours, and after that they start to die with scattered convection. They disappear completely after the 24th hour. The SSTSP3 and SSTSP6 both capture this fact. This shows that the SSTSP algorithms not only capture the large-scale features when a squall line is developed, but also have significant skill in the situation when no quasi-steady squall line is formed.

Next we consider  $a = 0.8$ , and observe that the mean propagating speed stays the same for all these experiments.

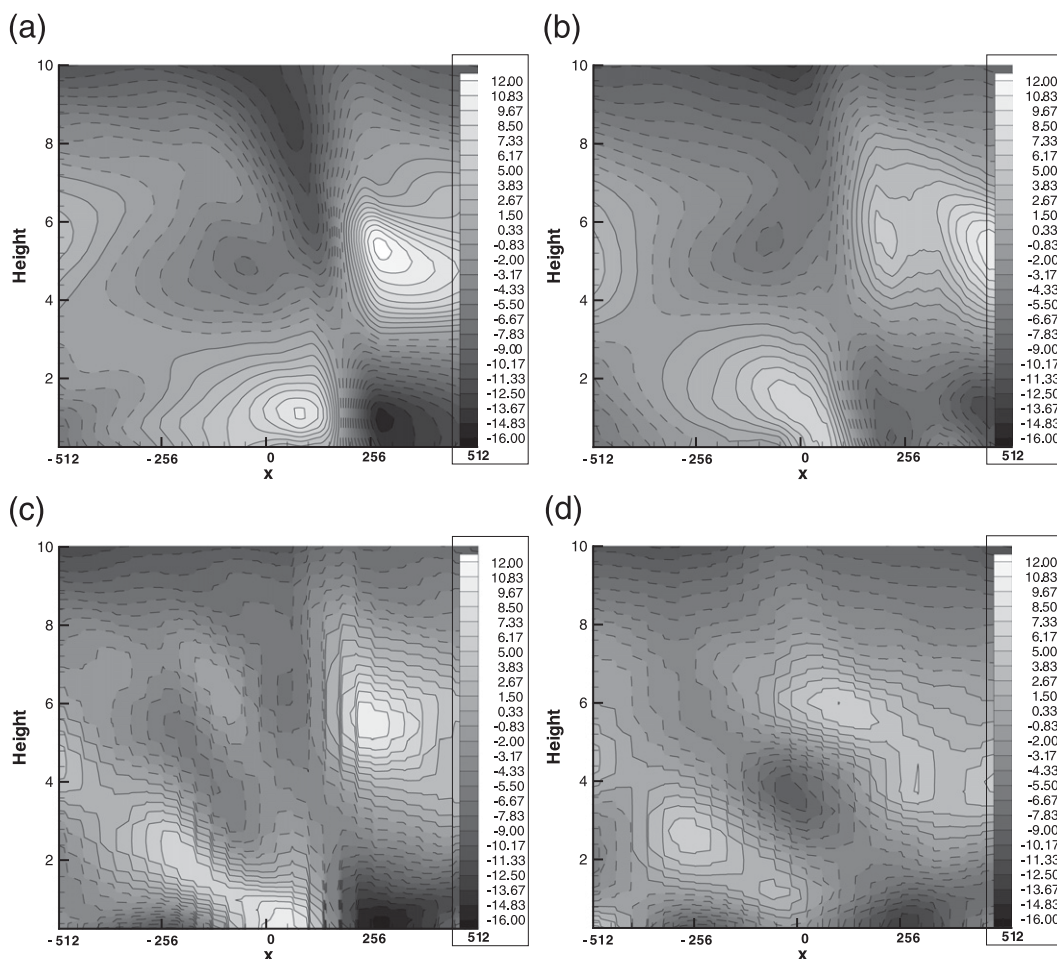


FIG. 11. The contours of the large-scale horizontal velocity  $\langle \bar{u} \rangle$  from different simulations with  $a = 0.5$ : (a) CRM squall-line simulation, (b) SP, (c) SSTSP3, and (d) SSTSP6.

The contour plots of surface precipitation are not included here for simplicity. As in section 3b for  $a = 1$ , the large-scale horizontal velocity and specific humidity are shown in Figs. 9 and 10, with the corresponding correlation shown in Table 3. We also compute the correlation compared with the ones from the original SP simulation and CRM simulation. The high correlation, above 0.75, of large-scale horizontal velocity and specific humidity between SSTSP2, SSTSP3, CRM, and SP shows that the new SSTSP algorithms capture the main large-scale feature of the squall line as in section 3b. There is even correlation skill above 0.6 for the SSTSP6 algorithm with  $1/36$  computational savings.

Finally, we address the case  $a = 0.5$ . The same environment is explored. Similarly, we observe that the mean propagating speed stays the same for all these experiments. The large-scale variables are shown in Figs. 11 and 12, with the corresponding correlation shown in Table 4. The same conclusion holds as in the earlier experiments and we observe the high correlation

of large-scale horizontal velocity and specific humidity for the SSTSP2 and SSTSP3 tests with similar moderate skill for SSTSP6 as reported earlier. The new efficient algorithm SSTSP3 saves the computational cost of these small-scale models by a factor of 9, and captures the main large-scale effects of all the squall-line experiments in a statistically accurate fashion.

#### d. Forced propagating squall lines

Above we showed that for a suite of quasi-steady squall-line experiment in a system-relative reference frame, the

TABLE 3. The correlation between the large-scale variables [defined in (27)] from these simulations when  $a = 0.8$ .

		SP	SSTSP2	SSTSP3	SSTSP6
$\langle \bar{u} \rangle$	SP	—	0.9011	0.8451	0.5924
	CRM	0.9057	0.8834	0.8145	0.6734
$\langle \bar{q}_w \rangle$	SP	—	0.9214	0.8512	0.7064
	CRM	0.8865	0.8432	0.7623	0.6352

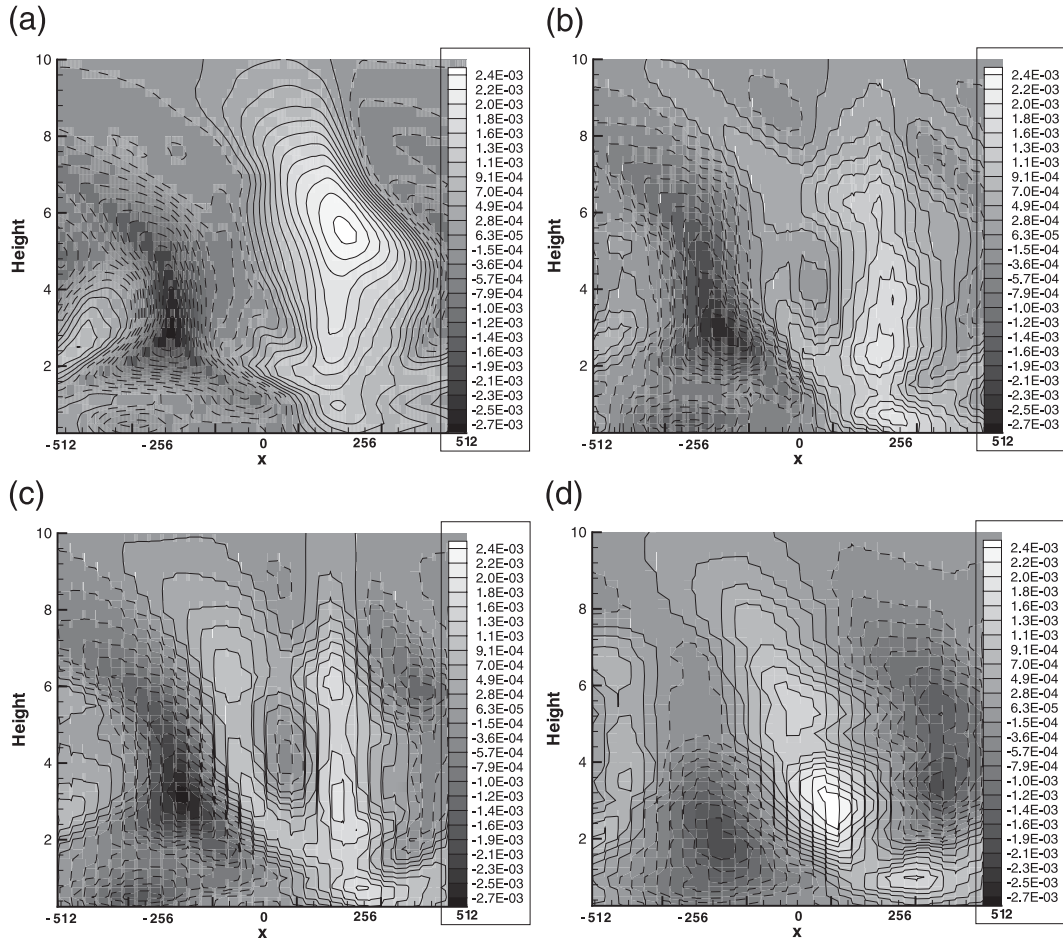


FIG. 12. As in Fig. 11, but for the large-scale specific humidity  $\langle \bar{q}_v \rangle$ .

SSTSP algorithms capture the large-scale features of the squall line in a statistically accurate way. In this subsection, we modify this experiment to obtain a propagating squall line, and check the performance of the new SSTSP algorithms as regards propagation speed.

The main setup of the squall-line experiment is the same. A different initial large-scale background shear is used for this experiment. It is the large-scale shear from the GARP GATE phase-III experiment and has been used in Grabowski (2006). The other difference between this experiment and the one in section 3b is that a periodic boundary condition is used on the large-scale model and large-scale forcing is applied for all the time. Unlike the earlier experiments, here we do not choose a flow-relative reference frame so the forced squall line propagates with an almost uniform speed. Because of the large-scale periodic boundary condition used, the squall line leaves the domain and returns at the other end.

We run the experiments for 3 days, the outer limit of squall-line persistence until the mesoscale background environment is expected to change. We can observe the

formation of a moving steady squall line with a fixed speed within the first 36 h. This can be inferred from the contour plots of the surface precipitation, as shown in Fig. 13. Propagating squall lines are obtained in all these experiments, and as shown in Table 5, both the SSTSP3 and SSTSP6 cases reproduce the squall-line speed in the CRM to within 10%. We notice that the active squall-line region in the SSTSP tests is broader, compared with the full-resolution CRM and SP tests. We believe this is because fewer spatial cells are used in the computation of SSTSP small-scale models; therefore, a larger spread over the coarse mesh of the large-scale model is needed

TABLE 4. The correlation between the large-scale variables [defined in (27)] from these simulations when  $a = 0.5$ .

		SP	SSTSP2	SSTSP3	SSTSP6
$\langle \bar{u} \rangle$	SP	—	0.8556	0.8023	0.6134
	CRM	0.8761	0.8573	0.7654	0.6248
$\langle \bar{q}_v \rangle$	SP	—	0.8932	0.8022	0.6573
	CRM	0.8635	0.8154	0.7235	0.6154

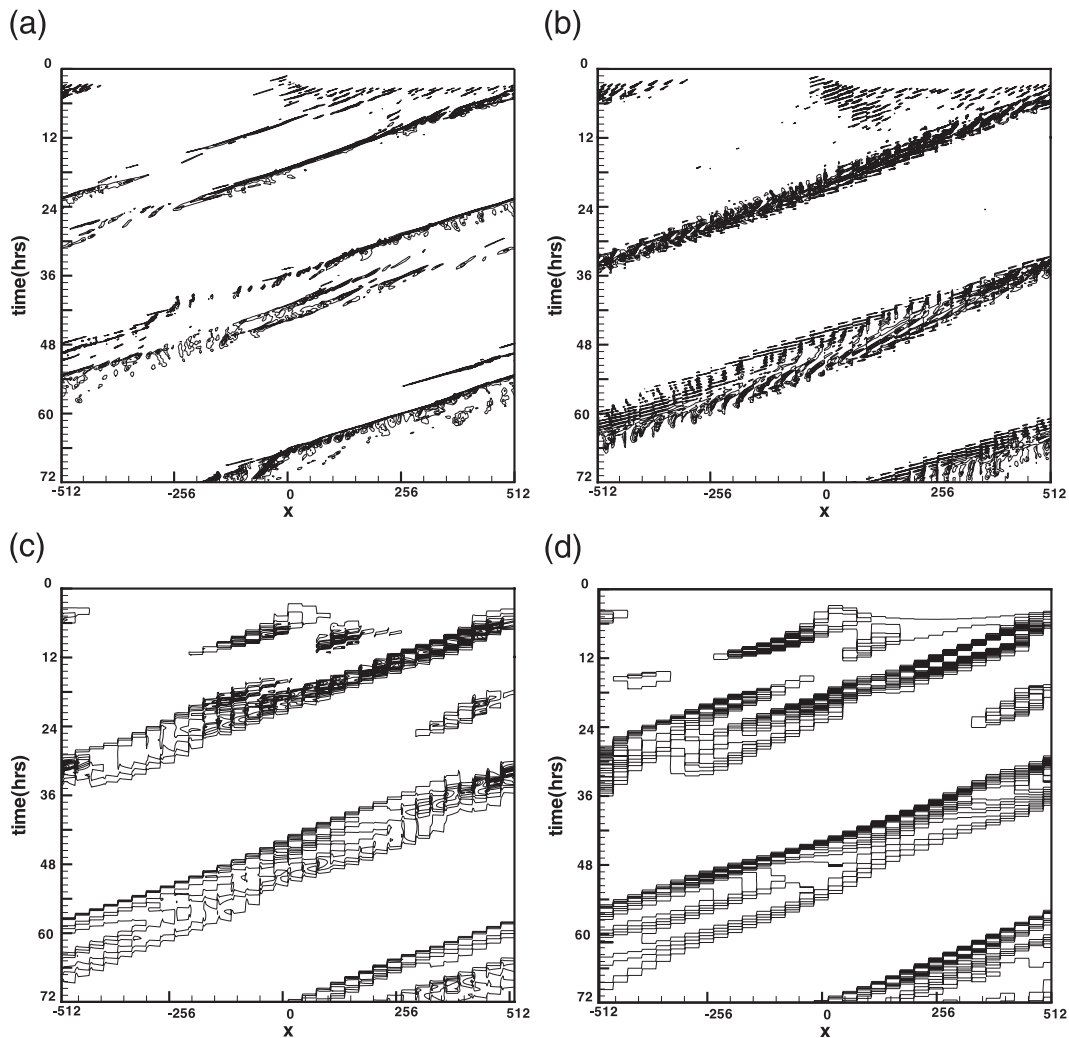


FIG. 13. The contours of the surface precipitation from different simulations for the forced propagating squall lines: (a) CRM squall-line simulation, (b) SP, (c) SSTSP3, and (d) SSTSP6.

to support propagation. We have checked the statistical large-scale features of these tests, and observed similar high correlations between the large-scale horizontal velocity and specific humidity as reported earlier in sections 3b and 3c.

#### 4. Conclusions

In section 2 we introduced the new efficient SSTSP algorithms, based on a modification of the original SP approach. By reducing the time interval of integration and the spatial periodic domain of the small-scale models with a factor of  $1/p$ , the computational cost can be reduced by a factor of  $1/p^2$ . A stringent test bed involving moist convection interacting with shear ranging from strong and weak free and forced propagating squall lines, to dying scattered convection was utilized to test

the performance of the algorithms. Comparisons with the full-resolved CRM results and the original fully resolved SP were presented throughout the test suite. In all tests both the SSTSP3 and SSTSP6 algorithms captured the squall-line speed with high accuracy as well as the process of dying scattered convection with weaker shears. The SSTSP3 algorithm was shown to capture the main large-scale features of the squall-line tests in a statistically accurate way with pattern correlation with the CRM above

TABLE 5. The jet max and squall-line speed of these five simulations for the propagating squall-line tests.

	CRM	SP	SSTSP2	SSTSP3	SSTSP6
Jet max (km)	14.1	14.1	14.1	14.1	14.1
Squall-line speed ( $\text{m s}^{-1}$ )	11.5	10.5	10	10	10

0.75 for both horizontal velocity and specific humidity, but with  $1/9$  the computational cost of the original SP. The computational cost was reduced significantly in this way. Even the extreme version of the algorithm, with  $p = 6$  and a  $1/36$  reduction in computational cost, retained significant skill throughout the test suite with pattern correlation with horizontal velocity and humidity above 0.6. This is surprising because in the SSTSP formulation, these are only six spatial grid cells and one small-scale time step for the small-scale model in SSTSP6; nevertheless, the small-scale model is chaotic enough in preconditioned regions of deep convection to support chaotic convective cells that communicate significant information to the large-scale model. For the strong squall line reported in section 3b, there is a significant eddy flux divergence driving horizontal momentum at large scales. While SSTSP3 and SP qualitatively capture the vertical dipole with the correct sign that occurred in the CRM result, the vertical location was displaced. The fact that this occurred with the fully resolved SP algorithm indicates that small-scale periodicity in the SP models is the probable source of this discrepancy. The SSTSP6 algorithm had too coarse resolution to reproduce this eddy flux divergence with any skill.

These new algorithms can be applied for parallel computations and implemented on supercomputers easily. Only 2D mesoscale models are tested in this paper. However, a 3D model will provide better statistics for SP models in the vicinity of a given location, so this approach might actually work even better in the case of a 3D large-scale outer model. Recently, the first two authors have developed a new asymptotic multiscale model for squall lines (Majda and Xing 2010). This multiscale model can be applied directly to these new algorithms to provide basic understanding of SSTSP algorithms as numerical methods. We leave all these for future research.

All of the results developed here point to the potential use of the SSTSP algorithms for ensemble prediction in limited area weather forecasting. The systematic development and skill of these algorithms developed here in the mesoscale atmosphere context suggest their potential use in other areas of climate atmosphere ocean science, such as for deep ocean convection, submesoscale eddies in the ocean mixed layer, etc., and merits an examination of the original SP algorithms for large-scale tropical dynamics (Grabowski 2002, 2003, 2004).

Recently (Majda 2007), systematic multiscale modeling was utilized to establish a link between SP algorithms on mesoscales and heterogeneous multiscale methods (HMM) developed in the applied mathematics literature for complex systems with widely disparate time scales (E and Engquist 2003; Vanden-Eijnden 2003; Engquist and Tsai 2005). In fact, the interpretation of the new SSTSP algorithms developed in

section 3d can be regarded as a reduced time, HMM method (Vanden-Eijnden 2003; Engquist and Tsai 2005). However, there are significant differences in the physics of mesoscale moist convection which has intermittency in space–time due to evolving chaotic moist and dry regions and only moderate values of scale separation  $\epsilon \cong 1/6-1/10$  (Majda 2007; Majda and Xing 2010), while the reduced time HMM time stepers are used for very different physical systems with wide scale separation  $\epsilon = 10^{-3}, 10^{-4}$ , and rapid local equilibration in time (Vanden-Eijnden 2003; Engquist and Tsai 2005). Thus, the skill reported here for the new SSTSP algorithms is through very different physical processes and time scales as compared with HMM. For further applications to anisotropic turbulence as mentioned above, it is very important to develop a basic understanding of the SSTSP algorithms and HMM as statistical numerical methods in an idealized context. Such a family of test models has been developed recently (Majda and Grote 2009).

*Acknowledgments.* The research of Andrew Majda is partially supported by ONR N0014-05-1-0164 and NSF DMS-0456713. Yulong Xing has been supported as a postdoctoral fellow through these grants.

#### REFERENCES

- Byers, H. R., and R. R. Braham, 1949: *The Thunderstorm—Report of the Thunderstorm Project*. U.S. Government Printing Office, 287 pp.
- E, W., and B. Engquist, 2003: The heterogeneous multiscale methods. *Comm. Math. Sci.*, **1**, 87–132.
- Engquist, B., and Y.-H. Tsai, 2005: Heterogeneous multiscale methods for stiff ordinary differential equations. *Math. Comput.*, **74**, 1707–1742.
- Grabowski, W. W., 1998: Toward cloud resolving modeling of large-scale tropical circulations: A simple cloud microphysics parameterization. *J. Atmos. Sci.*, **55**, 3283–3298.
- , 2001: Coupling cloud processes with the large-scale dynamics using the cloud-resolving convection parameterization (CRCP). *J. Atmos. Sci.*, **58**, 978–997.
- , 2002: Large-scale organization of moist convection in idealized aquaplanet simulations. *Int. J. Numer. Methods Fluids*, **39**, 843–853.
- , 2003: MJO-like coherent structures: Sensitivity simulations using the cloud-resolving convection parameterization (CRCP). *J. Atmos. Sci.*, **60**, 847–864.
- , 2004: An improved framework for superparameterization. *J. Atmos. Sci.*, **61**, 1940–1952.
- , 2006: Comments on “Preliminary tests of multiscale modeling with a two-dimensional framework: Sensitivity to coupling methods.” *Mon. Wea. Rev.*, **134**, 2021–2026.
- , and P. K. Smolarkiewicz, 1999: CRCP: A Cloud Resolving Convection Parameterization for modeling the tropical convecting atmosphere. *Physica D*, **133**, 171–178.
- Houze, R. A., Jr., 2004: Mesoscale convective systems. *Rev. Geophys.*, **42**, RG4003, doi:10.1029/2004RG000150.

- Jung, J.-H., and A. Arakawa, 2005: Preliminary tests of multiscale modeling with a two dimensional framework: Sensitivity to coupling methods. *Mon. Wea. Rev.*, **133**, 649–662.
- Khairoutdinov, M., D. Randall, and C. DeMott, 2005: Simulations of the atmospheric general circulation using a cloud-resolving model as a superparameterization of physical processes. *J. Atmos. Sci.*, **62**, 2136–2154.
- Lafore, J.-P., and M. W. Moncrieff, 1989: A numerical investigation of the organization and interaction of the convective and stratiform regions of tropical squall lines. *J. Atmos. Sci.*, **46**, 521–544.
- Majda, A. J., 2003: *Introduction to PDEs and Waves for the Atmosphere and Ocean*. Vol. 9, *Courant Lecture Notes in Mathematics*, American Mathematical Society, 234 pp.
- , 2007: Multiscale models with moisture and systematic strategies for superparameterization. *J. Atmos. Sci.*, **64**, 2726–2734.
- , and M. J. Grote, 2009: Mathematical test models for superparameterization in anisotropic turbulence. *Proc. Natl. Acad. Sci. USA*, **106**, 5470–5474, doi:10.1073/pnas.0901383106.
- , and Y. Xing, 2010: New multi-scale models on mesoscales and squall lines. *Comm. Math. Sci.*, **8**, 113–144.
- Moncrieff, M. W., 1992: Organized convective systems: Archetypal dynamical models, mass and momentum flux theory, and parameterization. *Quart. J. Roy. Meteor. Soc.*, **118**, 819–850.
- , and C. Liu, 2006: Representing convective organization in prediction models by a hybrid strategy. *J. Atmos. Sci.*, **63**, 3404–3420.
- Randall, D., M. Khairoutdinov, A. Arakawa, and W. W. Grabowski, 2003: Breaking the cloud parameterization deadlock. *Bull. Amer. Meteor. Soc.*, **84**, 1547–1564.
- Vanden-Eijnden, E., 2003: Numerical techniques for multiscale dynamical systems with stochastic effects. *Comm. Math. Sci.*, **1**, 385–391.
- Wu, X., and M. W. Moncrieff, 1996: Collective effects of organized convection and their approximation in general circulation models. *J. Atmos. Sci.*, **53**, 1477–1495.
- Wyant, M. C., M. Khairoutdinov, and C. S. Bretherton, 2006: Climate sensitivity and cloud response of a GCM with a superparameterization. *Geophys. Res. Lett.*, **33**, L06714, doi:10.1029/2005GL025464.